

# Sperm-Shaped Magnetic Microrobots: Fabrication using Electrospinning, Modeling, and Characterization

Islam S. M. Khalil\*, Ahmet Fatih Tabak<sup>†</sup>, Abdelrahman Hosney\*, Abdalla Mohamed\*, Anke Klingner\*, Maged Ghoneima<sup>§</sup> and Metin Sitti<sup>†</sup>

**Abstract**— We use electrospinning to fabricate sperm-shaped magnetic microrobots with a range of diameters from 50  $\mu\text{m}$  to 500  $\mu\text{m}$ . The variables of the electrospinning operation (voltage, concentration of the solution, dynamic viscosity, and distance between the syringe needle and collector) to achieve beading effect are determined. This beading effect allows us to fabricate microrobots with similar morphology to that of sperm cells. The bead and the ultra-fine fiber resemble the morphology of the head and tail of the sperm cell, respectively. We incorporate iron oxide nanoparticles to the head of the sperm-shaped microrobot to provide a magnetic dipole moment. This dipole enables directional control under the influence of external magnetic fields. We also apply weak (less than 2 mT) oscillating magnetic fields to exert a magnetic torque on the magnetic head, and generate planar flagellar waves and flagellated swim. The average speed of the sperm-shaped microrobot is calculated to be 0.5 body lengths per second and 1 body lengths per second at frequencies of 5 Hz and 10 Hz, respectively. We also develop a model of the microrobot using elastohydrodynamics approach and Timoshenko-Rayleigh beam theory, and find good agreement with the experimental results.

## I. INTRODUCTION

Researchers have suggested techniques and materials with morphologies and structures resembling those of living microorganisms. The flagellated swim of sperm cells and bacteria using single oscillating tail has been used to design and develop microrobots by Dreyfus *et al.* [1]. A microrobot that resembles the morphology of sperm cell has been fabricated using SU-8 polymer for the tail and a cobalt-nickel layer on the head to provide a dipole moment [2]. These microrobots are driven using external oscillating magnetic fields [3]. The flagellated swim of the *E. coli* bacteria has also been used to design artificial bacterial flagella with rigid helical structures by Zhang *et al.* [4]. These artificial bacterial flagella are driven by rotating magnetic fields using electromagnetic configuration and under microscopic guidance. Ye *et al.* [5] have used multiple flexible artificial flagella to increase the propulsive force of the microrobot, as opposed to microrobot with single flexible flagellum. It has also been demonstrated

This work was supported by funds from the German University in Cairo and the DAAD-BMBF funding project.

\*The authors are affiliated with the Faculty of Engineering and Material Science, the German University in Cairo, 11835 Egypt.

<sup>§</sup>The author is affiliated with the Mechatronics Engineering Department, Faculty of Engineering, Ain Shams University, 11566 Egypt.

<sup>†</sup>The authors are affiliated with the Physical Intelligence Department, Max Planck Institute for Intelligent Systems, Stuttgart, 70569 Germany.

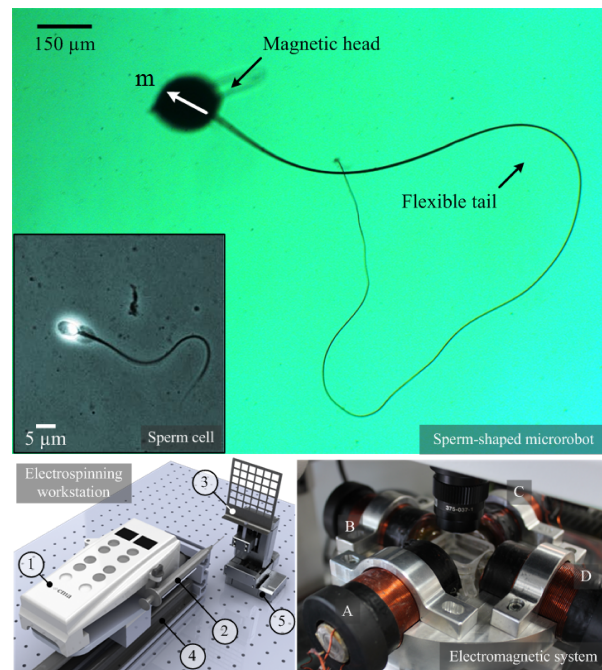


Fig. 1. A sperm-shaped microrobot is fabricated using electrospinning. This microrobot consists of a microbead and an ultra-fine fiber that resemble the morphology of a sperm cell. The microbead contains iron oxide nanoparticles (45-00-252 Micromod Partikeltechnologie GmbH, Rostock-Warnemuende, Germany) and provides magnetic dipole moment ( $\mathbf{m}$ ), whereas the fiber provides propulsive force when oscillating magnetic fields are applied. These fields are generated using an orthogonal configuration of electromagnetic coils (bottom-right inset). The sperm-shaped microrobot is fabricated using an electrospinning workstation (bottom-left inset). This workstation consists of a syringe pump ①, a syringe needle ②, a grounded collector ③, a linear motion stage ④, and a cartesian robot with 3 degrees-of-freedom ⑤. High voltage is supplied between the needle and the collector ⑥.

that the swimming speed increases linearly with the number of flagella. The propulsion mechanism of microscopic and miniature swimmers with flagellar motion have been modeled through measurement of the propulsive forces by Tony *et al.* [6] and Behkam *et al.* [7], respectively. However, the fabrication and modeling of the mechanism that governs the motion of biologically inspired microrobots remains a challenge. In this study we achieve the following:

- 1) fabrication of sperm-shaped microrobots (Fig. 1) using the beading effect of the electrospinning operation;
- 2) characterization of speed of the sperm-shaped micro-

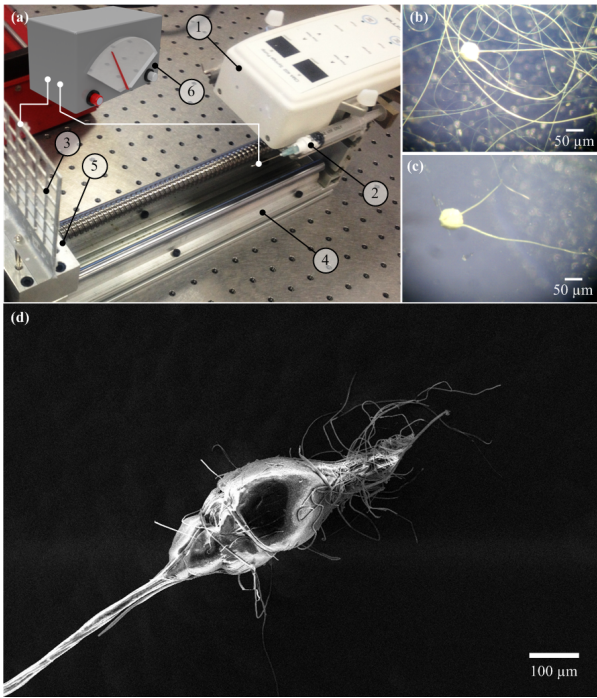


Fig. 2. Fabrication of sperm-shaped magnetic microrobots using electrospinning. (a) The electrospinning workstation consists of a syringe pump ①, a syringe needle ②, and a collector ③. The distance between the collector and the syringe needle is controlled using a linear motion stage ④ and a cartesian robotic system ⑤. The syringe needle and the collector are connected to a high-voltage power supply ⑥. (b) Beaded fibers are formed when electrical potential is increased to a few kilovolts. (c) The sperm-shaped microrobots are cut and separated from the fibers. The magnetic head provides directional control under the influence of the external magnetic fields, whereas the flexible tail provides propulsive force using a flagellated swim. (d) Scanning Electron Microscopy image of the sperm-shaped microrobot. *Please refer to the accompanying video that demonstrates the formation of beaded fibers using electrospinning.*

robot against the beating frequency of its flexible tail;

- 3) calculation of the rigid-body velocity vector of the sperm-shaped microrobot with respect to the input currents of the coils.

We present a technique to fabricate sperm-shaped magnetic microrobots using electrospinning. A solution of polystyrene in dimethylformamide, and iron oxide nanoparticles are used to form beaded ultra-thin fibers (Fig. 2). We also model the flagellated swim of the sperm-shaped microrobot. Majority of the numerical models for elastic slender tails are based on continuum elastohydrodynamics that directly couple the structural stresses with the hydrodynamic shear [8]. Other numerical models are based on bead-spring configuration models assuming a chain of beads connected with elastic elements under the influence of relatively complicated hydrodynamic drag [9]. Moreover, a dimensionless quantity ( $S_p$  number) is used to explain the relative importance of structural stresses to hydrodynamic stresses regardless of the modeling approach [1]. We use elastohydrodynamics approach with Timoshenko-Rayleigh beam model to study the swimming mechanism of the sperm-shaped microrobot.

TABLE I

PARAMETERS OF THE ELECTROSPINNING OPERATION. BEADED FIBERS ARE GENERATED USING THESE PARAMETERS AND SPERM-SHAPED MAGNETIC MICROROBOTS ARE CUT AND EXTRACTED FROM THE FIBERS.

Parameter	Value	Parameter	Value
Flow rate [ml/h]	3	Distance [cm]	10
Voltage [kV]	10	Polystyrene [%]	17
Dimethylformamide [%]	69	Iron oxide [%]	14

The remainder of this paper is organized as follows: Section II describes the proposed fabrication technique of the sperm-shaped microrobots based on the beading effect of the electrospinning operation. A numerical model based on elastohydrodynamics approach with Timoshenko-Rayleigh beam model is presented in Section III. Section IV provides our experimental frequency response characterization and a comparison between the experimental data and the numerical model. Finally, Section V concludes and provides directions for future work.

## II. FABRICATION OF THE SPERM-SHAPED MICROROBOTS USING ELECTROSPINNING

The sperm-shaped microrobots are fabricated by electrospinning [10] using a solution, i.e., polystyrene in dimethylformamide (Sigma-Aldrich, Taufkirchen, Germany) that is slowly injected through a needle via a syringe pump (CMA 402 Syringe Pump, CMA Microdialysis, Kista, Sweden). This solution is mixed with iron oxide nanoparticles (45-00-252 Micromod Partikeltechnologie GmbH, Rostock-Warnemuende, Germany). An electrical potential is applied using a high voltage power supply (521721, LD Didactic GmbH, Hürth, Germany) between the needle and the collector to introduce free charge at the liquid surface (Fig. 2(a)). The free charge generates electric stress that causes the liquid jet to stretch into fine filaments and accelerate away from the needle towards the collector. The liquid meniscus at the needle opening forms a conical shape when the electrical potential is increased to 10 kV. A liquid jet with high charge density is observed at the cone apex where the free charge is highly concentrated on the way from the needle to the collector. This liquid jet stretches via bending instability, and hence increases its surface area. Furthermore, the solvent of the polymer solution evaporates until the jet solidifies and the fibers are observed on the collector. The Rayleigh instability occurs if the diameter of the jet is very thin, and is in liquid state. This instability allows the jet to disintegrate into beads. *Please refer to the accompanying video that demonstrates the formation of beaded fibers using electrospinning.*

The transition from formation of beads, beads with fibers, and pure fibers depends on increasing the initial concentration of the polymer [10]. Beaded fibers (Fig. 2(b)) are formed on the collector for solutions with intermediate viscosity. We extract the beaded fibers from the metallic collector. Then, the collected structures are cut and extracted using tweezers under high magnification. One cut is made close to the bead

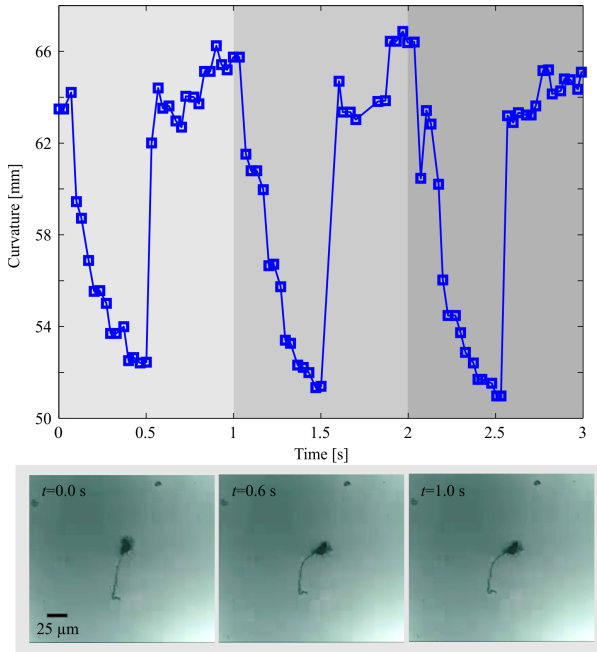


Fig. 3. Flexibility of the tail of the sperm-shaped microrobot is demonstrated under the influence of oscillating magnetic field at 1 Hz. This flexibility enables a non-reciprocal deformation and flagellated swim. The curvature is calculated at each time instant for 3 time periods.

and the second cut depends on the desired length of the tail. This procedure leads to a geometry that resembles the morphology of a sperm cell, as shown in Figs. 2(c) and (d). Table I provides the parameters of the electrospinning operation that are used throughout our experimental work to fabricate the sperm-shaped microrobots. The volume of the bead with major diameter of  $100\ \mu\text{m}$  is one order of magnitude larger than the volume of the tail with  $200\ \mu\text{m}$  and  $20\ \mu\text{m}$ , in length and diameter, respectively. Therefore, homogenous distribution of iron oxide nanoparticles is assumed and the magnetic dipole moment of the bead should dominate the magnetic response of the sperm-shaped microrobot. The beads provide the magnetic dipole, whereas the propulsive force is generated by the ultra-thin fiber using a flagellated swim. Motion of the sperm-shaped microrobot is controlled using an electromagnetic system with orthogonal configuration Fig. (1).

We demonstrate experimentally that the sperm-shaped microrobot breaks the time-reversal symmetry and swims using a wave propagation. Fig. 3 provides a representative experiment of the wave propagation through the flexible tail of the microrobot. In contrast to flapping a rigid tail that cannot result in propulsion, our microrobot is flexible and wave propagation is demonstrated in Fig. 3. We calculate the curvature of the tail at representative time instants under the influence of oscillating field of 1 Hz. Another proof-of-concept experiment is provided in Fig. 4 on the flagellated propulsion of the sperm-shaped microrobot. In this representative experiment, the weak (2 mT) magnetic fields

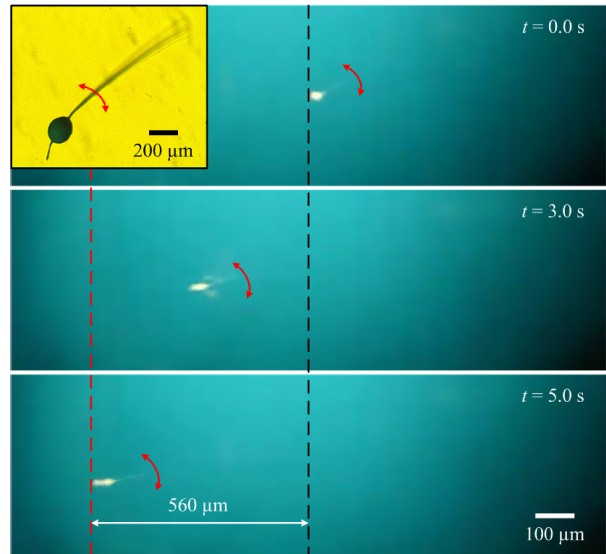


Fig. 4. A representative flagellated swim of the sperm-shaped microrobot under the influence of weak (2 mT) oscillating magnetic fields. The oscillating magnetic fields are applied at frequency of 10 Hz. The swimming speed of the sperm-shaped microrobot is  $112\ \mu\text{m/s}$ . The inset shows a microscopic image of the microrobot. The black and red dashed lines indicate the travel of the sperm-shaped microrobot. The red arrow indicates the oscillation of the flexible tail. Please refer to the accompanying video that demonstrates the flagellated swim of the sperm-shaped microrobot.

are oscillated at 10 Hz to allow for the flagellated swim of the microrobot. We observe that the microrobot swims at an average speed of  $112\ \mu\text{m/s}$ . The interaction between elasto-hydrodynamics (of the head and tail) and the Magneto-hydrodynamics (of the electromagnetic configuration) is analyzed using a numerical model.

### III. NUMERICAL MODELLING OF THE SPERM-SHAPED MAGNETIC MICROROBOT

The numerical model of the sperm-shaped microrobot consists of three components: elasto-hydrodynamics for dynamic tail deformation based on Timoshenko-Rayleigh beam theory [12], [13], Magneto-hydrodynamics based on the Biot-Savart law for electromagnetic coils [14], [15], and rigid-body kinematics based on transient Stokes-flow approach with force-free swimming conditions [16], [17], [18]. Each component utilizes resistive force coefficients based on resistive-force-theory [19], [20] to calculate the resultant hydrodynamic forces exerted on the elastic tail and the magnetic body of the microrobot (regarding to the elastic deformation or rigid-body motion). The equation of motion of the microrobot based on the force-free swimming condition is given by

$$\begin{bmatrix} \mathbf{V} \\ \mathbf{\Omega} \end{bmatrix} = -\mathbf{B}_{\text{sw}}^{-1} \begin{bmatrix} \mathbf{F}_{\text{mag}} + \mathbf{F}_{\text{add}} \\ \mathbf{T}_{\text{mag}} + \mathbf{T}_{\text{add}} \end{bmatrix}, \quad (1)$$

where  $\mathbf{V}$  and  $\mathbf{\Omega}$  are the linear and angular rigid-body velocities of the microrobot, respectively. Further,  $\mathbf{F}_{\text{mag}}$  and  $\mathbf{F}_{\text{add}}$  are the magnetic force and inertial force due to added mass and history effects on the microrobot, respectively.

TABLE II

SPECIFICATION OF ONE ELECTROMAGNETIC COIL OF THE MAGNETIC SYSTEM. THE MAGNETIC FIELDS ( $\mathbf{B}$ ) ARE MEASURED AT THE CENTER OF THE WORKSPACE USING A CALIBRATED 3-AXIS DIGITAL TESLAMETER.  $r_i$  AND  $r_o$  INDICATE THE INNER AND OUTER RADIUS OF THE COILS, RESPECTIVELY.  $D$ ,  $l_t$ , AND  $t$  ARE THE DIAMETER OF THE HEAD, LENGTH OF THE TAIL, AND THICKNESS OF THE TAIL, RESPECTIVELY.  $E$ ,  $\nu$ , AND  $G$  ARE THE MODULUS OF ELASTICITY, POISSON RATIO, AND SHEAR MODULUS, RESPECTIVELY.

Parameter	Value	Parameter	Value
Length [mm]	800	Number of turns	3200
$r_i$ [mm]	5	$r_o$ [mm]	20
$ \mathbf{B}(\mathbf{P}) $ [mT]	2	$\nabla \mathbf{B}(\mathbf{P}) $ [T.m <sup>-1</sup> ]	1.62
$D$ [ $\mu\text{m}$ ]	100	$E$ [GPa]	3 – 3.5
$l_t$ [ $\mu\text{m}$ ]	800	$t$ [ $\mu\text{m}$ ]	20
$\nu$	0.34	$G$ [GPa]	1.1 – 1.3

Further,  $\mathbf{T}_{\text{mag}}$  and  $\mathbf{T}_{\text{add}}$  are the magnetic torque and the inertial torque due to added mass and history effects acting on the microrobot, respectively. In addition,  $\mathbf{B}_{\text{sw}}$  is the resistance matrix of the microrobot that consists of the resistance matrices of the body and the tail, and is given by

$$\mathbf{B}_{\text{sw}} = \mathbf{B}_b + \mathbf{B}_t, \quad (2)$$

where  $\mathbf{B}_b$  and  $\mathbf{B}_t$  are the resistance matrices of the body and tail, respectively.  $\mathbf{B}_b$  is represented using

$$\mathbf{B}_b = \begin{bmatrix} \mathbf{D}_{\text{tran}} & -\mathbf{D}_{\text{tran}}\mathbf{S}_b \\ \mathbf{S}_b\mathbf{D}_{\text{tran}} & \mathbf{D}_{\text{rot}} \end{bmatrix}. \quad (3)$$

In (3),  $\mathbf{D}_{\text{tran}}$  and  $\mathbf{D}_{\text{rot}}$  are diagonal matrices of translational and rotational resistive force coefficients of the body, and  $\mathbf{S}_b$  is the skew symmetric-matrix signifying the cross-products. In (2),  $\mathbf{B}_t$  is the resistance matrix of the tail and is given by

$$\mathbf{B}_t = \int_0^{l_t} \begin{bmatrix} \mathbf{RCR}^T & -\mathbf{RCR}^T\mathbf{S}_t \\ \mathbf{S}_t\mathbf{RCR}^T & -\mathbf{S}_t\mathbf{RCR}^T\mathbf{S}_t \end{bmatrix} dl \quad (4)$$

where  $l_t$  is the length of the sperm-shaped microrobot. Further,  $\mathbf{C}$  and  $\mathbf{R}$  are the diagonal matrices of the local resistive force coefficients and the rotation matrix from local Frenet-Serret coordinate frames to the inertial frame of reference of the microrobot, respectively, along the elastic tail [21]. Furthermore,  $\mathbf{S}_t$  is the skew symmetric-matrix signifying the cross-products. The magnetic force ( $\mathbf{F}_{\text{mag}}$ ) and torque ( $\mathbf{T}_{\text{mag}}$ ) acting on the microrobot are given by

$$\begin{bmatrix} \mathbf{F}_{\text{mag}} \\ \mathbf{T}_{\text{mag}} \end{bmatrix} = \begin{bmatrix} \mathbf{R}_{\text{sw}}^T V (\mathbf{M} \cdot \nabla) \mathbf{B} \\ V \mathbf{M} \times \mathbf{B} \end{bmatrix}, \quad (5)$$

where  $V$  is the volume of the magnetic nano-particles of the microrobot and  $\mathbf{M}$  is its magnetization in the frame of the laboratory. Further,  $\mathbf{B}$  is the magnetic flux density vector generated by the electromagnetic configuration. The frame of the electromagnetic system and the frame of the microrobot are related using the rotation matrix ( $\mathbf{R}_{\text{sw}}$ ). The

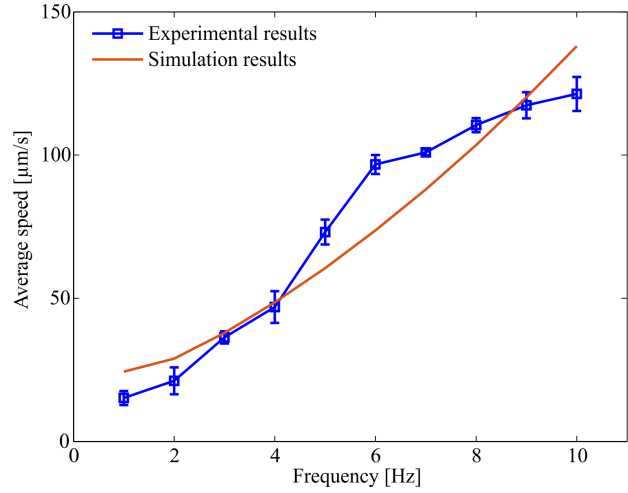


Fig. 5. Experimental and simulation frequency response of sperm-shaped microrobots. The average speed is calculated from 10 trials at each frequency. The maximum swimming speed is observed at frequency of 10 Hz. The simulation results (red line) are calculated using (1). Oscillating magnetic fields are generated by applying the currents inputs (14) and (15) to the 4 electromagnetic coils. Please refer to the accompanying video that shows the flagellated swim of the microrobot at representative frequencies.

components of the electromagnetic fields generated using our electromagnetic configuration are calculated using [15]

$$B_x = \left(\frac{5}{4}\right)^{\frac{3}{2}} \frac{B_0}{4\pi} \int_0^{2\pi} \left(1 - \frac{y}{r} \cos \theta - \frac{z}{r} \sin \theta\right) F_0^{-\frac{3}{2}} d\theta, \quad (6)$$

where  $B_x$  is the magnetic field along  $x$ -axis and  $r$  is the inner-radius of the electromagnetic coil. Moreover,  $B_0$  is given by

$$B_0 = \left(\frac{4}{5}\right)^{\frac{3}{2}} \frac{\mu_0 N I_c}{r}. \quad (7)$$

In (7),  $\mu_0$ ,  $N$ , and  $I_c$  are the permeability of the iron core, number of turns of each coil, and the input current to each of the electromagnetic coils, respectively. Further,  $F_0$  is given by

$$F_0 = \left(\frac{x}{r}\right)^2 + \left(\frac{y}{r} - \cos \theta\right)^2 + \left(\frac{z}{r} - \sin \theta\right)^2. \quad (8)$$

The magnetic field along  $y$ -axis ( $B_y$ ) is given by

$$B_y = \left(\frac{5}{4}\right)^{\frac{3}{2}} \frac{B_0}{4\pi} \int_0^{2\pi} \left(\frac{x \cos \theta}{r F_0^{\frac{3}{2}}}\right) d\theta. \quad (9)$$

Finally, the magnetic field along  $z$ -axis ( $B_z$ ) is given by

$$B_z = \left(\frac{5}{4}\right)^{\frac{3}{2}} \frac{B_0}{4\pi} \int_0^{2\pi} \left(\frac{x \sin \theta}{r F_0^{\frac{3}{2}}}\right) d\theta. \quad (10)$$

The magnetic field gradient is calculated numerically using (6), (9), and (10) to determine the magnetic force (5) exerted on the magnetic dipole of the microrobot.

The structural deformation in the frame of the microrobot with reference ( $\varphi$ ) is calculated based on the Timoshenko-Rayleigh beam model to take the vibration effect and large

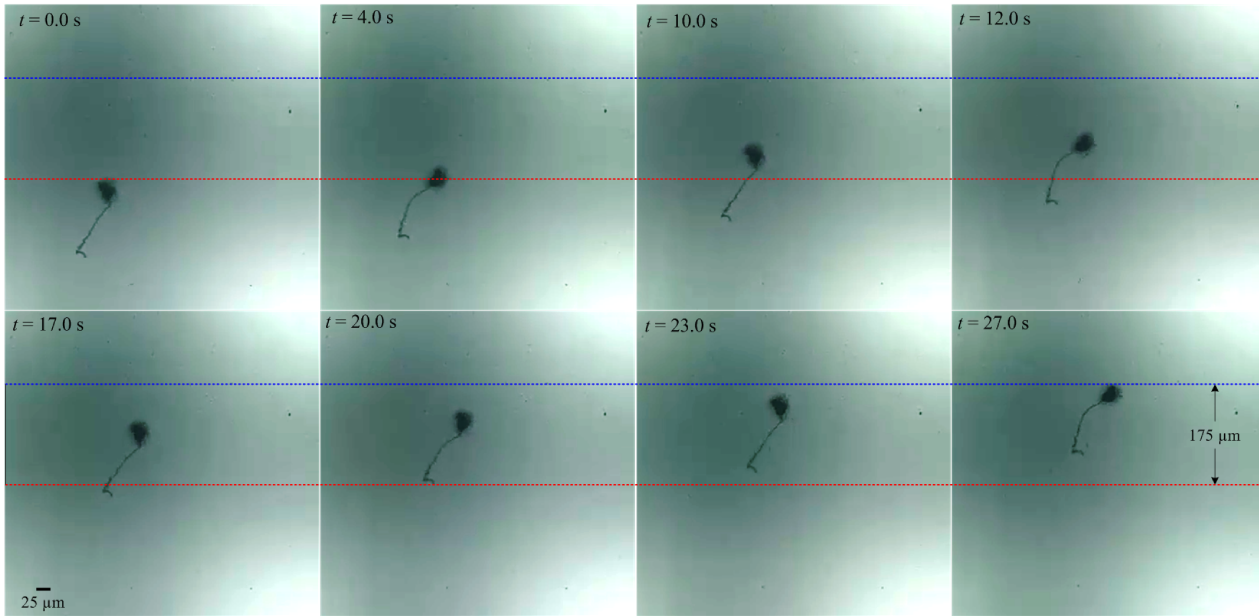


Fig. 6. A representative motion control of a sperm shaped microrobot under the influence of weak (less than 2 mT) oscillating magnetic fields at frequency of 1 Hz. The sperm-shaped microrobot swims at an average speed of 7  $\mu\text{m/s}$ . The red and blue dashed lines represent the distance traveled by the microrobot. Please refer to the accompanying video that demonstrates the flagellated swim of the sperm-shaped microrobot.

deformations into account for high actuation frequencies and axial shear forces. This frame is required to obtain the local time-dependent Frenet-Serret frames in (4). The Timoshenko-Rayleigh beam model is given by [12], [13]

$$\frac{\partial^2}{\partial x^2} \left( EI \frac{\partial^2 \varphi}{\partial x^2} \right) + f_x \frac{\partial^2 \varphi}{\partial x^2} + m \frac{\partial^2 \varphi}{\partial t^2} + \frac{Jm}{kAG} \frac{\partial^4 \varphi}{\partial t^4} - f_y = \left( J + \frac{mEI}{kAG} \right) \frac{\partial^4 \varphi}{\partial t^2 \partial x^2} + \frac{J}{kAG} \frac{\partial^2 f_y}{\partial t^2} - \frac{EI}{kAG} \frac{\partial^2 f_y}{\partial x^2}, \quad (11)$$

where  $E$  is the Young's modulus and  $G$  is the shear modulus. Further,  $A$ ,  $I$ ,  $m$  and  $J$  are the cross-sectional area, second moment of area, mass per unit length, and moment of inertia per unit length, respectively, and  $k$  is the shape correction coefficient for Timoshenko's beam theory. We consider that the tail is flexible but not extensible, and hence the length of the tail ( $l_t$ ) remains constant. Therefore, the net local hydrodynamic force acting on the flexible tail is calculated using

$$\begin{bmatrix} f_x & f_y & f_z \end{bmatrix}^T = \begin{bmatrix} \mathbf{RCR}^T & -\mathbf{RCR}^T \mathbf{S}_t \end{bmatrix} \begin{bmatrix} \mathbf{V} \\ \boldsymbol{\Omega} \end{bmatrix}. \quad (12)$$

We only use the first two elements on the right hand side. The joint between the body and the flexible tail is rigid leading to zero deformation and zero deflection at this point. The boundary conditions for reaction force and reaction torque are calculated as the sum of all of the forces acting on the body. Finally, the transient hydrodynamic force due to the added-mass and history effects are calculated using [16]

$$\begin{bmatrix} \mathbf{F}_{\text{add}} \\ \mathbf{T}_{\text{add}} \end{bmatrix} = \begin{bmatrix} \Phi \int_{-\infty}^t \frac{d\mathbf{V}}{dt} \frac{d\tau}{\sqrt{t-\tau}} - \frac{2}{3} \pi R^3 \rho_l \frac{d\mathbf{V}}{dt} \\ \mathbf{S}_b \mathbf{F}_{\text{add}} \end{bmatrix}, \quad (13)$$

where  $\rho_l$  is the density of the medium and  $R$  is the radius of the body. In (13),  $\Phi$  is calculated using,  $\Phi = 6R^2 \sqrt{\pi \mu \rho_l}$ , and  $\mu$  is the dynamic viscosity of the medium (glycerine is used throughout our experimental work). The input currents on the coils are modeled as:

$$I_{cA} = I_{cC} = I_{\text{max}} \sin \left( \Omega_z + \frac{\pi}{4} \cos(2\pi ft) \right), \quad (14)$$

where  $I_{cA}$  and  $I_{cC}$  are the current inputs to electromagnetic coils A and C, respectively. Further,  $I_{\text{max}}$ ,  $f$ , and  $\Omega_z$  are the maximum input current, frequency, and the  $z$ -component of the rigid body rotation, respectively. The current inputs to electromagnetic coils B ( $I_{cB}$ ) and D ( $I_{cD}$ ) are given by

$$I_{cB} = I_{cD} = I_{\text{max}} \cos \left( \Omega_z + \frac{\pi}{4} \cos(2\pi ft) \right). \quad (15)$$

Our model is verified by comparing its results to the experimental frequency response of the microrobot.

#### IV. CHARACTERIZATION OF THE FREQUENCY RESPONSE AND MOTION CONTROL OF THE MICROROBOT

The magnetic field are adjusted with respect to the orientation of the microrobot throughout the experiments. Once we implement the equation of motion (1), we employ a custom modified forward-Euler time integration method based on trapezoidal rule with  $l_t$  in (4) discretized by 250 mesh nodes,  $\theta$  in (6), (9), and (10) is discretized by 5000 mesh nodes with equal spacing. Moreover, the maximum time step for each full period of sinusoidal coil currents are set to  $1/(20000f)$  seconds. All the initial conditions for structural deformation and rigid-body kinematics are set to zero. The initial direction of the magnetization ( $\mathbf{M}$ ), is set to  $[-1 \ 0 \ 0]^T$ . The oscillating magnetic field is generated

with a frequency range of 0 Hz to 10 Hz. The physical parameters of simulations are provided within Table II.

The response of the sperm-shaped microrobot to weak oscillating magnetic field is characterized experimentally using an electromagnetic system (Fig. 1). This system consists of an orthogonal array of electromagnetic coils. The electromagnetic configuration surrounds a reservoir that contains the sperm-shaped microrobots and is mounted on an aluminum base to dissipate the generated heat of the coils. This configuration is mounted on a microscopic unit (MF Series 176 Measuring Microscopes, Mitutoyo, Kawasaki, Japan). The position of the sperm-shaped microrobot and the oscillation of its tail are determined using a high-speed camera (avA1000-120kc, Basler Area Scan Camera, Basler AG, Ahrensburg, Germany) and our feature tracking algorithm [11]. The four electromagnetic coils are independently supplied with current inputs using electric drivers (MD10C, Cytron Technologies Sdn. Bhd, Kuala Lumpur, Malaysia) and controlled via an Arduino control board (Arduino UNO - R3, Arduino, Memphis, Tennessee, U.S.A).

The frequency response of the sperm-shaped microrobot is determined by applying uniform magnetic fields within the center of the workspace of the electromagnetic configuration. This uniform magnetic field is generated by applying the current inputs (14) and (15). We calculate the average swimming speed from 10 trials at each frequency. The maximum swimming speed is observed at frequency of 10 Hz, as shown in Fig. 5. The average speed increases almost linearly with the frequency of the fields. This experiment indicates that the break-out frequency of the microrobot is greater than 10 Hz. Our frequency range is limited with the frequency response of the electromagnetic coils. Therefore, the maximum frequency is 10 Hz. Fig. 6 provides a representative motion control experimental result of a sperm-shaped microrobot at oscillating field of 1 Hz. The swimming speed of the microrobot is calculated to be 7  $\mu\text{m/s}$ . Please refer to the accompanying video that demonstrates the flagellated swim of the sperm-shaped microrobot.

## V. CONCLUSIONS AND FUTURE WORK

We use electrospinning to fabricate sperm-shaped microrobots. Iron oxide nanoparticles are incorporated to the head of the microrobot to provide a magnetic dipole moment and enable flagellated swim and directional control under the influence of weak oscillating magnetic field. The microrobot swims (without magnetic field gradient) by wave propagation that breaks the time-reversal symmetry and a swimming speed of approximately 1 body lengths per second is achieved, at frequency of 10 Hz. In addition, we use elasto-hydrodynamics approach with Timoshenko-Rayleigh beam theory to study and model the deformation of the microrobot, and we find good agreement with the experimental results.

As part of future studies, the sperm-shaped microrobots will be used to target and penetrate human astrocytoma cell line U-373MG *in vitro* using ultrasound feedback [22]. The uptake rate and the internalization mechanisms of the microrobots will be also studied. In addition, the propulsive

force of the sperm-shaped microrobot will be characterized by incorporating a microforce sensing probe to our system.

## REFERENCES

- [1] R. Dreyfus, J. Baudry, M. L. Roper, M. Fermigier, H. A. Stone, and J. Bibette, "Microscopic artificial swimmers," *Nature*, vol. 437, October 2005.
- [2] I. S. M. Khalil, H. C. Dijkslag, L. Abelmann, and S. Misra, "MagnetoSperm: A microrobot that navigates using weak magnetic fields," *Applied Physics Letters*, vol. 104 (223701), June 2014.
- [3] K. Youakim, M. Ehab, O. Hatem, S. Misra, and I. S. M. Khalil, "Paramagnetic microparticles sliding on a surface: characterization and closed-loop motion control," in *Proceedings of the IEEE International Conference on Robotics and Automation (ICRA)*, pp. 4068-4073, Seattle, Washington, USA, May 2015.
- [4] L. Zhang, J. J. Abbott, L. Dong, B. E. Kratochvil, D. Bell, and B. J. Nelson, "Artificial bacterial flagella: fabrication and magnetic control," *Applied Physics Letters*, vol. 94 (064107), February 2009.
- [5] Z. Ye, S. Régnier, and M. Sitti, "Rotating magnetic miniature swimming robots with multiple flexible flagella," *IEEE Transactions on Robotics and Automation*, vol. 30, no. 1, pp. 3-13, February 2014.
- [6] E. L. Tony, S. Yu, and A. E. Hosoi, "Experimental investigations of elastic tail propulsion at low Reynolds number," *Physics of Fluids*, vol. 18 (091701), September 2006.
- [7] B. Behkam and M. Sitti, "Design methodology for biomimetic propulsion of miniature swimming robots," *Transactions of the ASME Journal of Dynamic Systems Measurement and Control*, vol. 128, no. 1, pp. 36-43, March 2006.
- [8] C. H. Wiggins, D. Riveline, A. Ott, and R. E. Goldstein, "Trapping and wiggle: elasto-hydrodynamics of driven microfilaments," *Biophysical Journal*, vol. 74, no. 2, pp. 1043-1060, February 1998.
- [9] E. Gauger, and H. Stark, "Numerical study of a microscopic artificial swimmer," *Physics Review*, vol. 74, pp. 021907 (1-10), August 2006.
- [10] D. Li and Y. Xia, "Electrospinning of nanofibers: reinventing the wheel?," *Advanced Materials*, vol. 16, no. 14, pp. 1151-1170, July 2004.
- [11] I. S. M. Khalil, K. Youakim, A. Sánchez, S. Misra "Magnetic-based motion control of sperm-shaped microrobots using weak oscillating magnetic fields", in *Proceedings of the IEEE International Conference of Robotics and Systems (IROS)*, pp. 4686-4691, September 2014.
- [12] T. Kaneko, "On Timoshenko's correction for shear in vibrating beams," *Journal of Physics D: Applied Physics*, vol. 8, no. 16, pp. 1927-1936, November 1975.
- [13] H. E. Rosinger and G. Ritchie, "On Timoshenko's correction for shear in vibrating isotropic beams," *Journal of Physics D: Applied Physics*, vol. 10, no. 11, pp. 1461-1466, August 1977.
- [14] H. Choi, J. Choi, G. Jang, J.-oh Park, and S. Park, "Two-dimensional actuation of a microrobot with a stationary two-pair coil system," *Smart Materials and Structures*, vol. 18, pp. 055007 (1-9), March 2009.
- [15] R. Beiranvand, "Analyzing the uniformity of the generated magnetic field by a practical one-dimensional Helmholtz coils system," *Review of Scientific Instruments*, vol. 84, pp. 075109 (1-11), 2013.
- [16] L. D. Landau and E. M. Lifshitz, "Fluid Mechanics," *Pergamon Press*, 1987.
- [17] G. I. Taylor, "Analysis of the swimming of microscopic organisms," *Proceedings of Royal Society*, vol. 209, no. 1099, pp. 447-461, November 1951.
- [18] A. F. Tabak and S. Yesilyurt, "Improved kinematic models for two-link helical micro/nanoswimmers," *IEEE Transactions on Robotics*, vol. 30, no.1, pp. 14-25, February 2014.
- [19] C. Brennen and H. Winet, "Fluid mechanics of propulsion by cilia and agella," *Annual Review of Fluid Mechanics*, vol. 9, pp. 339-398, January 1977.
- [20] H. C. Berg, "Random walks in biology," *Princeton University Press*, 1993.
- [21] A. J. Hanson and H. Ma, "Quaternion frame approach to streamline visualization," *IEEE Transactions on Visualization and Computer Graphics*, vol. 1, no. 2, pp. 164-174, June 1995.
- [22] I. S. M. Khalil, P. Ferreira, R. Eleutério, C. L. de Korte, and S. Misra, "Magnetic-Based closed-loop control of paramagnetic microparticles using ultrasound feedback," in *Proceedings of the IEEE International Conference on Robotics and Automation (ICRA)*, pp. 3807-3812, Hong Kong, China, June 2014.